Journal of Applied Fluid Mechanics, Vol. 11, No. 1, pp. 79-94, 2018.
Available online at www.jafmonline.net, ISSN 1735-3572, EISSN 1735-3645.
DOI: 10.29252/jafm.11.01.27831

Shielding Gas Coaxial Jet Pipes Numerical Study of a Vertical Laser Welding Process of AZ91 Magnesium Alloy

C. Boughanmi[1†], S. Bannour[1,2], H. Mhiri[1] and P. Bournot[2]

[1] *UTTPI, Thermodynamics and Thermal Unit Industrial Process (UTTPI) Ecole Nationale d'Ingénieurs de Monastir ENIM, 5000 Monastir, Tunisia.*
[2] *IUSTI, Technopole of Château-Gombert, 5 city Enrico Fermi, 13013 Marseille, France.*

†*Corresponding Author Email:chiraz.boughanmi@gmail.com*

(Received April 2, 2017; accepted August 15, 2017)

ABSTRACT

The laser welding of magnesium alloys, largely used in many fabrication applications, has gained considerable interest especially in aerospace, electronics, automotive industry etc. Unfortunately, this process is associated to an undesired phenomenon which is "oxidation". For this reason, a good shielding system of the welding zone is of major importance. This paper presents a numerical study using computational fluid dynamics (CFD) of a laser welding process employing a moving volumetric heat source. Starting with the turbulence model validity, a parametric study of this welding process in a vertical position aiming to optimize the design of protection gas device, the gas jet inclination, the appropriate welding direction and the gas type is, then, proposed. The optimum parametric combination ensuring the largest gas coverage area is the one where the shielding gas is Argon, supplied by the coaxial nozzles at a downward inclination angle with respect to the laser beam axis, and a downward welding direction.

Keywords: Laser welding; Shielding gas; Coaxial impinging jet; Numerical study; Volume fraction.

NOMENCLATURE

b, c	focal radii of the laser beam
Cp	specific heat capacity
D	diameter of the outer pipe
d	diameter of the inner pipe
e	maximum depth
g	gravity constant
$\bar{h}(R)$	average convective wall heat transfer coefficient
h	convective heat transfer coefficient
k	thermal conductivity
$\overline{Nu}(R)$	average Nusselt number
Nu(r)	local Nusselt number
P_l	power of the laser beam
Q	heat laser source
R	radius
r	radial coordinate
T	temperature
t	time
u_i,u_j,u,v,w	velocity components
x_i,x_j,x,y,z	cartesian coordinates
φ	convective flux density
$\Phi(R)$	heat flux on a circular plate of *R* radius
β	thermal expansion
ΔH	latent heat of fusion
η	efficiency
μ	dynamic viscosity
θ	Jet pipe inclination

Subscripts

g	gas
w	wall
ext	exterior (ambient)
wel	welding

1. INTRODUCTION

Having interesting characteristics, laser welding is becoming nowadays one of the most attractive joining technologies used in many industrial applications relevant to deep penetrations and high

welding speeds, circumscribed heat affected zones and low thermal loads (Haferkamp *et al*. 2000). Laser has a wide variety of beam generating sources which helps to join most of the engineering materials from metals to polymers with undoubted high quality results and a good process efficiency. The interaction between the beam and the matter is a complex phenomenon having a great influence on the manufacturing process. Among the by-products of this interaction is the plasma plume which causes undesired effects on the laser beam such as energy absorption and defocusing by the ionization of the gas surrounding the welding zone on the one hand, and by the ionization of the metal vapors coming from the base material on the other hand. Thus, the need to use shielding gases in order to control the base metals reactivity with respect to the welding atmosphere and plasma plume formation. This shielding gas must be inert to the base material components and high temperatures; it should also have high ionization potential components to help the reduction of the plasma amount during the welding process (Cao *et al*. 2006).

In this context, some researches focused on the shielding gas effect on the quality of the laser weld. This gas is chosen based on parameters such as: its nature, the geometry of the nozzle, jet angle, jet velocity, etc. Bannour *et al*. (2012) had investigated numerically and experimentally the effects of different flow rates, using a simple circular nozzle, on the horizontal welding pool dimensions and temperature distributions. They reported that the shielding gas affects all the weld characteristics such as the shape, penetration and efficiency. These conclusions were also reached by Lin and Chen (2001). Sathiya *et al*. (2012) examined experimentally the strength, depth and width of the weld with different shielding gases (He, Ar and N2) derived from a simple nozzle. They concluded that good results can be achieved depending on the laser beam power, the travel speed and the focal position. With a similar study, Qiang *et al*. (2014) noticed that the molten depth of welding is deeper and the width is narrower using Nitrogen, but to restrain plasma the mixed gas of He, Ar and N2 is suitable. Thus, using different shielding gases, Sun *et al*. (2017) examined the porosity in the laser welds. They concluded that Nitrogen allows the maximum elimination of pores. Given this importance, it is clear that the shielding gas process needs many investigations and requires a precise analysis in order to optimize its use.

In order to improve the area of the shielding gas on the heat affected zone, we leaned on the optimization of the jet flows. This process is non other than a jet impacting a heated plate. This type of jet is a topic of considerable interest. Understanding the physical phenomena of these flow types with or without heating is of major importance. This involves complex phenomena of fluid mechanics and heat transfer.

Various studies dealing with those impinging jet flows have been conducted without consideration for the welding process. For instance, Meena *et al*. (2016) investigated experimentally the effect of the nozzle geometry on the heat transfer and reported that the circular orifice provides the highest amount of heat transfer compared to the elliptical, square and triangular orifices. Moreover, Trinh *et al*. (2016) found that the circular orifice on the hemisphere causes a higher heat transfer rate than the simple circular one, and Buchlin (2011) discovered that the three lobes' nozzle prevails thermally over the four lobes' nozzle, which yields a similar performance to the round nozzle. Muthukannan *et al*. (2016) investigated numerically a single vertical slot jet on a heated block mounted on the bottom wall. It is observed that the presence of a solid block increases the overall unsteadiness in the flow. Sagot *et al*. (2008) achieved a series of experiments followed by a numerical study treating the thermal transfer of a simple circular impinging jet. The investigation has led to an average Nusselt number correlation.

Among the nozzle shapes studied is the coaxial nozzle. Many research reported a significant progress achieved when dealing with the coaxial free jets, which improves the region of the potential core and the turbulence intensity at the nozzle outlet due to the presence of mixing of the primary and secondary streams. Coaxial flows are used in novel domains for instance in the non-Newtonian nanofluid in heat exchangers (Bahiraei *et al*. 2014, Bahiraei 2016, Bahiraei *et al*. (2017a, 2017b)).

However, the effects of the coaxial shape of impinging jets have always remained a raw subject and more investigations on this subject are still required. Some of the rare works or more accurately the only ones were those carried out by Celik *et al*. (2012, 2009), who studied the heat flux of an impinging coaxial jet for different nozzle diameter ratios. Based on the study findings, the heat transfer on the stagnation zone differs from one case to another. Far away from that zone, the coaxial impinging jet, without regard to the diameter ratios, and the simple circular jet have the same behaviour.

Regarding the jet flows of the shielding gas for the laser welding process, the optimization of the design of the protection gas device as well as the gas flow in the laser welding is not yet fully elucidated. Grevey *et al*. (2005) recorded and analyzed experimentally the pressure created by the shielding gas flow and the operating parameters of a horizontal welding process. The results are obtained for two nozzles: the external pipe contains the shielding gas and the inner one contains the laser beam. As an optimized device, they proposed a diffuser that surrounds the two nozzles to avoid oxidation. In the same context, Ancona *et al*. (2005) have focused on the effect of two different shielding gas delivery systems: a conical nozzle and a two-separate nozzle on the horizontal laser welding process of AA5083 Aluminum–Magnesium alloy. It turned out experimentally that the more effective one was the two-separate pipes configuration.

Yokohara *et al*. (2016) investigated numerically and experimentally the Argon shielding gas supplying of a ring nozzle for a large area in the vertical laser welding of Titanium. The k- ε turbulence model was used in the numerical study, but neither the welding pool modeling nor the heat effect, have been

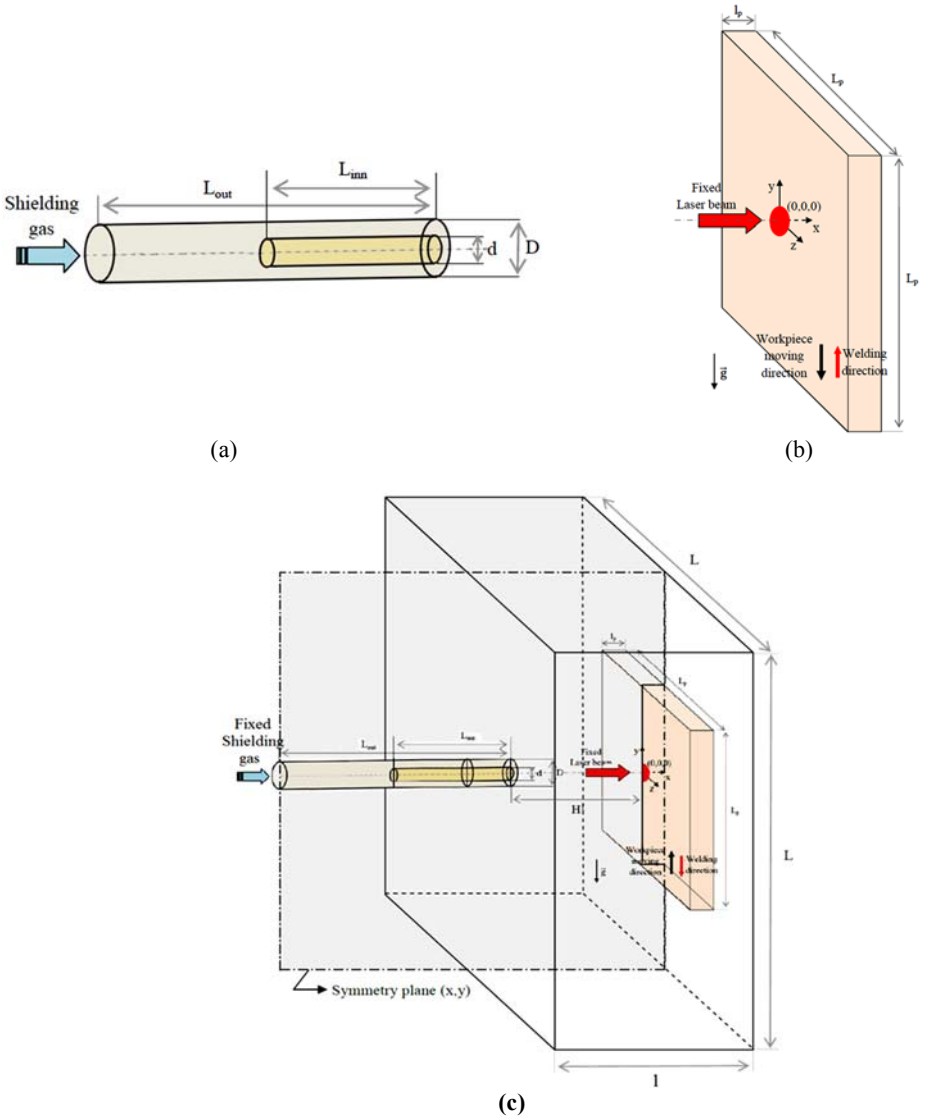

Fig. 1. Geometric configuration: (a) coaxial shielding gas tubes, (b) Workpiece, (c) Assembled model.

considered. A numerical parametric study was also conducted by Tani *et al*. (2007) using the k- ε turbulence model in order to optimize the simple circular gas distribution around the welding zone acting on the jet angle inclination and gas type, but still, without the modeling of the welding pool.

However, two configurations have not been yet elucidated: firstly, coaxial nozzles for the shielding gas, secondly a vertical laser welding process with a simple or coaxial shielding gas nozzles.

Therefore, the main purpose of this work is a numerical study of the shielding gas coaxial jet during the laser welding process which is modeled with a prescribed heat input as a mathematical model for the weld heat sources. The first part of this paper is dedicated to comparing the effect of the coaxial nozzles configuration with that of the simple circular nozzle, on the welding coverage zone.

In the vertical position of the welding process, the buoyancy and gravity forces cause the non-symmetry phenomena of the upper and the lower part of the flux. So, the inclination of the shielding gas jet (downward and upward) and the position of the welding pool (downward and upward) need to be explored. In this context, the second part of our paper is devoted to make this assessment. In the last part, the effect of the gas density on the shielding gas area is studied. Thus, two inert gases were compared: Argon and Helium.

This study will help us establish the optimal combination ensuring the best extent shielding gas covered area.

2. NUMERICAL MODELING

2.1 Geometric Configuration

The coaxial jet of interest is generated by two coaxial tubes as shown in Fig. 1.(a). The flow enters into the outer tube. After a specific distance, it enters the inner one. From this point, the flow runs in a parallel

way in both tubes until the exit of the nozzles where these two parallel flows give rise to two jets forming together the coaxial jet. Diameters and lengths of the outer and the inner tubes are respectively noted D, d, L_{out} and L_{inn}. The workpiece is made of AZ91 (Table 2) and is a rectangular parallelepiped with l_p of thickness. Its upper and lower faces are square with L_p length sides as shown in Fig. 1.(b). The piece to weld is placed vertically at a distance H from the coaxial impinging jet exit which is placed horizontally as shown in Fig. 1.(c). It should be noted that both considered tubes are of very small dimensions compared to the ambient domain, in which the flow opens at the atmospheric conditions (T=27°C).

The ambient domain length L enables to move the workpiece on each side of the y-axis in order to simulate the movement during the welding process.

All mentioned dimensions are given in Table 1. This three-dimensional configuration is developed with reference to the experimental data reported by Celik and Eren (2009).

Table1 Geometric dimension value

Dimension	Value (mm)
D	13.8
d	4.83
L_{inn}	220.8
L_{out}	441.6
L	431
l	H+3D
L_p	215.5
l_p	2

2.2 Mathematical Formulation

The mathematical formulation of the model is performed taking into account the following assumptions:

- The configuration being symmetric according to the median plane (x,y). To expedite the computations, only the half of the model will be considered (Fig.1(c)) (Hozoorbakhsh *et al.* 2016 and Chang *et al.* 2013).
- The flow regime is assumed to be turbulent (Re≥10000) and unsteady.
- The jet emitted horizontally is axisymmetric.
- The fluid is assumed to be incompressible with constant thermo-physical properties except for its density. The Boussinesq approximations are adopted. In this notion, the fluid density, in all solved equations, is considered as a constant, apart from the term of buoyancy in the momentum equation in which it is treated as: $\rho = \rho_{ref}(1-\beta(T-T_{ref})g)$. (Wang *et al.* 2007, Abderrazak *et al.* 2009, Chang *et al.* 2013).
- The surface of the weld pool is considered flat (Yokohara *et al.* 2016, Hozoorbakhsh *et al.* 2016, Chang *et al.* 2013, Bannour *et al.* 2012, Abderrazak *et al.* 2009, Wang *et al.* 2007). So, the complex physical mechanisms related to the keyhole formation and stability are disregarded.
- The temperature of the work piece is initially fixed at 300K.
- The laser beam and coordinate system origin (0,0,0) are fixed and placed in the centre of the upper workpiece surface as shown in Fig.1 (b).
- The workpiece moves according to the y-axis with a constant velocity (v_{wel}).

Taking account of the above assumptions, in the Cartesian coordinate system, general conservation equations are written as follows:

Continuity equation:

$$\frac{\partial \rho}{\partial t}+\frac{\partial(\rho u_i)}{\partial x_i}=0 \qquad ; i=1,2,3 \tag{1}$$

Momentum conservation equation :

$$\frac{\partial(\rho u_i)}{\partial t}+\frac{\partial(\rho u_i u_j)}{\partial x_j}=-\frac{\partial p}{\partial x_i}+\frac{\partial}{\partial x_j}(\mu\frac{\partial u}{\partial x_j})-\frac{\mu}{K}(u_i-u_{wel\ i})+\rho g_i\beta(T-T_{ref})$$

; i, j=1,2,3 (2)

Energy conservation equation:

$$\rho C_p(\frac{\partial T}{\partial t}+(u_i-u_{wel_i})\frac{\partial T}{\partial x_i})=\frac{\partial}{\partial x_i}(k\frac{\partial T}{\partial x_i})+Q-\frac{\partial}{\partial x_i}(\rho u_i \Delta H)$$

; i=1,2,3 (3)

Fusion latent heat, ΔH, is considered as a melting/solidification model based on the enthalpy-porosity method (Voller and Prakash 1987). It is established by adding a heat source term in the energy conservation equation, which is updated according to an appropriate latent updating form during each interaction within a time step. And the permeability term, K (In momentum equations), is related to the liquid volume fraction via the Koseny-Carman equation (Bennon and Incropera 1987). It allows us to have a harmonious velocity transition from zero in the solid zone to a high value in the fully liquid region for the fixed-grid numerical method. Using the term permeability and the source term, the system of governing equations becomes valid for both the fluid and solid phases. This avoids the need to track the solid-fluid interface and the implementations of new boundary conditions at the interface. Akbari *et al.* 2014, Bannour *et al.* 2012, Abderrazak *et al.* 2009 and Wang *et al.* 2007 presented similar studies, using the same method.

These equations reveal additional unknown terms, hence the need to use turbulence models enabling the mathematical resolution of the equation system.

2.3 Turbulence Models

Numerical simulations were conducted using three turbulence models in order to find the most suitable one for the flow field prediction; A comparison is performed between the efficiency of two high-

Reynolds number turbulence models, respectively the Realizable k-ε model (Shih *et al.* 1995) and the RNG k- ε model (Choudhury 1993) coupled to the near wall model approach namely "Enhanced Wall Treatment", and a low-Reynolds number turbulence model, the SST k-ω model. This last model was developed to effectively blend the accurate and robust k-ω model formulation in the near wall zone with the k- ε model free stream independence in the far field. Thus, it includes in the ω equation a damped cross-diffusion derivative term; it performs a modification of the turbulent viscosity definition to account for the turbulent shear stress transport; additionally, the model constants are different from those of the standard k-ω model (Menter 1994).

2.4 Boundary Conditions

The boundary conditions for solving the governing equations are as follows:

- A velocity inlet is set at the outer pipe entry (See Fig.3).
- The plane (x,y) represents the symmetry plane of the computational domain(See Fig.3).
- The atmospheric pressure is set at the ambient domain boundaries (See Fig.3).
- At the inlet, the temperature was specified to be uniform and equal to the ambient temperature T_{amb}.

Regarding the boundary conditions at the workpiece, during the laser welding process, the beam supplies an energy that acts on the upper surface and in the keyhole which is formed between the two parts to be welded. This results in a temperature increase which will be modeled with a prescribed heat input as a mathematical model for the weld heat sources, based on the Gaussian space distribution of the power density.

The heat source expression, based on finite volume methods (FVM), has been the subject of several studies making a lot of developments on the computing performance in the computational fluid dynamics (Akbari *et al.* 2014, Wang *et al.* 2011; Abderrazak *et al.* 2009). The volumetric heat source used in this work was proposed by Goldak *et al.* (1984), used by Chang *et al.* (2013), Bannour *et al.* (2012), Wang *et al.* (2011), Abderrazak *et al.* (2009) etc, and is expressed as follows:

$$Q = \frac{3P_l\eta}{\pi ebc}\exp\left(-\frac{3x^2}{e^2}\right)\exp\left(-\frac{3y^2}{b^2}\right)\exp\left(-\frac{3z^2}{c^2}\right) \quad (4)$$

With : P_l is the total power of the laser beam, □ is the efficiency kept constant at 80% , b and c are taken to be equal to the focal radii of the laser beam and e is the maximum depth.

This volumetric heat source term is identified with Q in Eq.(3).

The surface tension force, buoyancy force and electromagnetic force (Lorentz force) present the conducting forces for the welding pool convection. The convection induced by the surface tension is known as thermo-capillary driven flow or Marangoni effect which is caused by surface temperature gradients. In the magnesium alloy composition, the surface-active agent is absent, that means that the surface tension will drop when the temperatures increase. So, the thermal gradient of the surface tension is negative hence the choice of the negative Marangoni in this study. Therefore, the flow moves from hot to cold (Abderrazak *et al.* 2009). The Marangoni convection acts against the surface tension on the weld pool's top surface and is the principal fluid flow and heat transfer driving force (Ha and Kim 2005, Fan *et al.* 2001 and Limmaneevichitr *et al.* 2000). The workpiece boundary conditions are as follows (Bannour *et al.* 2012, Abderrazak *et al.* 2009 and Akbari *et al.* 2014):

- At the workpiece upper surface (see Fig.2):
  - The liquid region (weld pool) (see Fig.2):

$$u = 0; \mu\frac{\partial v}{\partial x} = -\frac{\partial\gamma}{\partial T}\frac{\partial T}{\partial y};\ u = 0; \mu\frac{\partial v}{\partial x} = -\frac{\partial\gamma}{\partial T}\frac{\partial T}{\partial y}; \quad (5)$$

$\frac{\partial\gamma}{\partial T}$: The temperature coefficient of surface tension.

  - The solid region (see Fig.2):

$$u = 0; v = v_{wel}; w = 0 \quad (6)$$

- At the workpiece lower surface (see Fig.2):
  - Convection heat transfer conditions are applied:

$$\phi_{ext} = h_{ext}(T_{ext} - T_w) \quad (7)$$

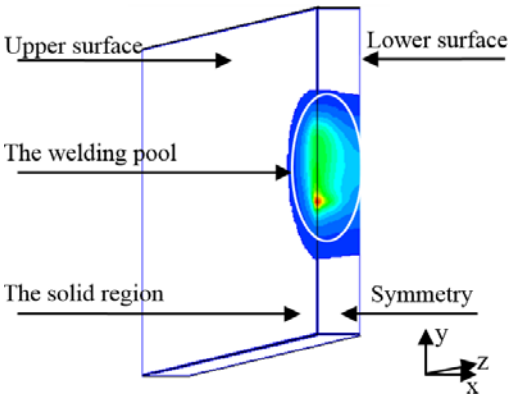

Fig. 2. Schematic of the workpiece.

2.5. Thermophysical Properties of the Workpiece.

The workpiece material is the AZ91 magnesium alloy. Based on the Mg-Al system (9% Aluminum) which presents good mechanical properties, it is the most widely used magnesium alloy. Its thermo-physical properties are summarized in Table 2.

2.6. Computational Details

Calculations were carried out using the computational fluid dynamics software Fluent. The numerical resolution is based on the finite volume method (FVM). To model the laser beam welding

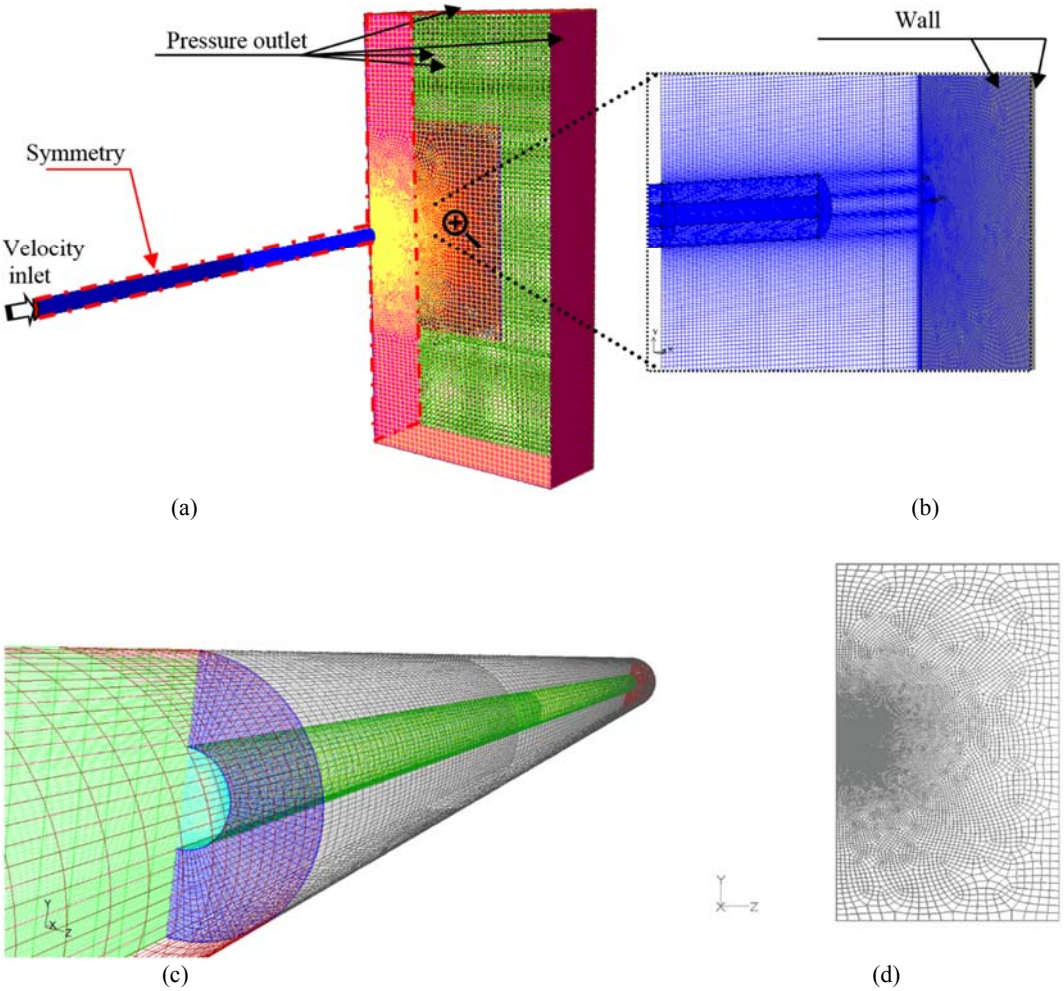

energy with a volumetric heat source expressed by Eq. (4), a code was implemented in Fluent based on a User-defined function (UDF) written in C language. Thus, in order to model the translational moving workpiece, the steady-state approximation Moving reference frame (MRF) model was used. The translational velocity is fixed as a constant on the y-axis and zero for the rest. To predict the shape and motion of the different phases, the Volume of fluid (VOF) multiphase method was applied (Cho *et al*. 2014, Bannour *et al*. 2012, Li *et al*. 2014).

Table 2 Material properties of AZ91 magnesium alloy (International Magnesium Association)

Property	Unit	Value
Density of solid phase(ρ)	kg m^{-3}	1810
Specific heat of solid phase (C_{ps})	J $kg^{-1}K^{-1}$	1020
Thermal conductiv.of solid phase (k_s)	$Wm^{-1}K^{-1}$	146
Absorption coefficient (α)	/	0.3
Melting heat (L_m)	J kg^{-1}	3.7×10^{5}
Solidus temperature (T_s)	K	740
Liquidus temperature (T_l)	K	870
Dynamic viscosity (μ)	kg $m^{-1}s^{-1}$	1.72×10^{-5}
Thermal expansion coefficient (β)	K^{-1}	1.1×10^{-5}
Surf. tension temperature coeff. (γ)	N.m^{-1}	-0.64×10^{-3}
Gravitational acceleration (g)	ms^{-2}	9.81
Boiling temperature (T_v)	K	1380

A grid sensitivity study is carried out in order to evaluate the solution sensitivity to the grid refinement. Three grid meshes were tested during the simulations constituted respectively of 800000 cells, 990000 cells and 1360000 cells. The difference between the obtained results for meshes 2 and 3 is lower than 1%. However, compared to the first, this difference reaches 5%. So, based on the computing time weakness, the selected grid is the second one (formed by 990000 cells). Fig. 3(a) shows an overall view of the 3D computational domain mesh. A detailed view of the mesh at the coaxial tubes is given in Fig.3 (b) and (c) and the piece to be welded in Fig.3 (b) and (d). In fact, the geometric complexity of the configuration incited us to decompose the domain into several sub domains. Thus, a hexahedral non-uniform multi-zone mesh composed of several blocks connected by interface boundary conditions is used. In order to have correct predictions using the SST turbulence model and with applying the near-wall model approach 'Enhanced Wall Treatment' coupled to the k- ε turbulence models, the required value of the important factor (y+) is of the order of 1 (y+≈1). This term (y^+) known as the dimensionless wall distance, measures the fluid variables gradient at every cell; lower gradient means a better model accuracy. It is commonly

used in the boundary layer theory and in the definition of the wall law. Therefore, to obtain this value, a spatial grid adaptation was applied at the impingement surface and at the coaxial tubes' walls. The accuracy of the numerical results was ensured by requiring that all residuals reduced to 10^{-5}. The time step used was fixed to 10^{-6}s.

3. RESULTS AND DISCUSSIONS

3.1. Turbulence Model Validity

The aim, in this section, is to study the validity of the turbulence models described in section (2.3) for two configurations of the impinging jet: circular single and coaxial. A comparison is carried out between the present numerical results of the two configurations of impinging jet nozzle: simple and coaxial with those of a simple impinging jet obtained by Sagot *et al.* (2008) and those of a coaxial impinging jet obtained by Celik *et al.* (2012). Thus, the investigation is based on the local and average Nusselt number results.

Taking into account the same operating conditions of the cited authors, the welding process will not be considered. However, for the impingement surface, the temperature was assumed to be uniform and equal to T_w.

All the other surfaces were considered adiabatic. At the inlet of the solution domain, the temperature was specified to be uniform and equal to the ambient temperature T_{amb}.

Moreover, the jet exit is circular. Therefore, the distribution of the local and average Nusselt numbers on the plate is also considered circular. Then, the Nusselt numbers distribution will be a function of the dimensionless r/D ratio (Jambunathan *et al.* 1992, Celik *et al.* 2012).

In accordance with these conditions, the convective flux density is described as follows:

$$\varphi = h(T_W - T_{jet}) \tag{8}$$

and, the local Nusselt number is given by this expression:

$$Nu(r) = \frac{h(r)D}{k_g} \tag{9}$$

The corresponding average Nusselt number is defined as:

$$\overline{\mathrm{Nu}}(\mathrm{R}) = \frac{\bar{h}(R)D}{k_g} \tag{10}$$

Where the average convective wall heat transfer coefficient is expressed as follows:

$$\bar{h}(R) = \frac{1}{\pi R^2}\frac{\phi(R)}{T_W - T_{jet}} \tag{11}$$

And the heat flux on a circular area of radius R is written as:

$$\phi(R) = \int_0^R \varphi(r) 2\pi r dr \tag{12}$$

The numerical simulations were performed for various geometric parameters H/D corresponding to the exit jet-to-plate distance and various Reynolds numbers. The different studied cases for the turbulence model validity are summarized in Table 3.

Table 3 Studied cases for the turbulence model validity

	Pipe geometry	Re	H/D	Turbulence model		
Case A	Simple	23000	2	SST k-ω	Rng k- ε	Real. k- ε
Case B	Coaxial	10000	4	SST k-ω	Rng k- ε	Real. k- ε
Case C	Coaxial	10000	2	SST k-ω		
Case D	Coaxial	20000	2	SST k-ω		
Case E	Coaxial	20000	4	SST k-ω		
Case F	Coaxial	23000	2	SST k-ω		

- For the simple jet, the numerical results are compared to the numerical and experimental data of Sagot *et al.* (2008) for Re=23000 and H/D=2.

Figure 4 shows the comparison between the local Nusselt number, obtained using various turbulence models (Case A in Table 3) and those numerically obtained by Sagot *et al.* (2008). It can be seen from this figure that, when the RNG or the Realizable k- ε turbulence model is used, the decrease of the local Nusselt numbers is monotonic and the secondary maximum is not noticed at all. This result confirms that these two turbulence models are not appropriate to predict such a flow configuration. However, The SST k–ω turbulence model provides a correct prediction of the local Nusselt number distribution ensuring generally a good agreement with the Sagot *et al.* (2008) obtained numerical result. In fact, there is a good prediction of the local Nu at: the stagnation point, the first peak and the secondary peak. The local Nu at the first peak is approximately 3.5% higher than that of the stagnation point. It corresponds to the maximum rate of heat transfer occurring at the proximity of the lateral edge r/D=0.5 of the nozzle. The first peak is attributed to the important turbulence intensity at the nozzle edge (Lee and Lee 2000). The secondary peak is situated at r/D=2. It is assigned to the transition from the laminar to the turbulent boundary layer in the spreading wall jet (Lee and Lee 2000). This transition is triggered by the pressure gradient disappearance that occurs in the stagnation region. Thus, the pressure gradient stabilizes the laminar boundary layer, in spite of the high levels of turbulence in the free jet flow (Lee and Lee 2000).

Thereby, despite the modifications made in the RNG and in the Realizable k- ε models compared to the standard k- ε model, it is noticed that it was not enough to predict the flow and especially predict the laminar/turbulent transition of the flow. However, the advantage of the SST k–ω model in term of performance for a larger class of flows is that it gives a better prediction of flows with low Reynolds numbers, laminar/turbulent transition and shear layers (see section 2.3).

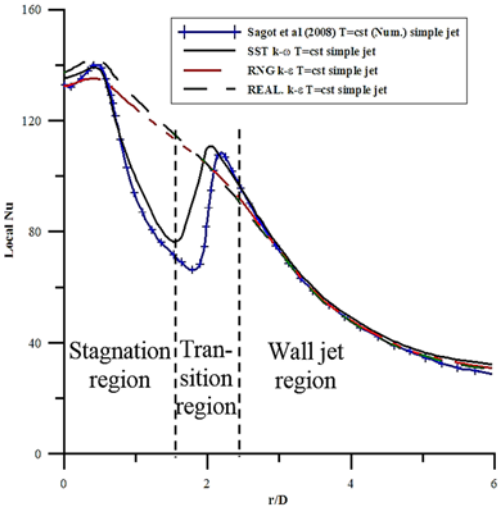

Fig. 4. Local Nusselt numbers (*Nu*) of simple jet obtained with various turbulence models (case A) compared to literature result for Re= 23 000 and H/D = 2.

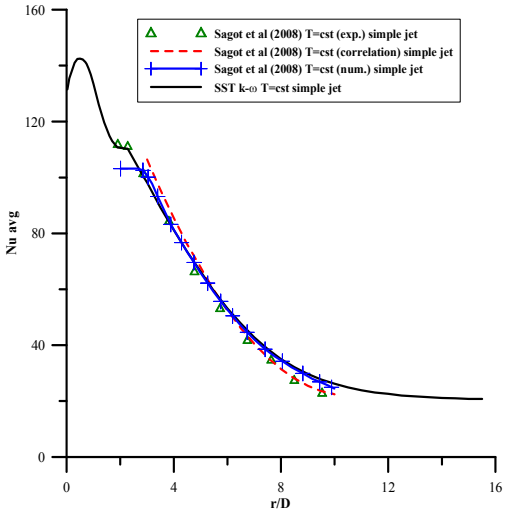

Fig. 5. Average Nusselt numbers ($\overline{Nu}$) of simple jet (case A: SST k-ω model) compared to literature results for Re=23 000 and H/D=2.

As mentioned by Lee and Lee (2000), the evolution of the local Nusselt number also allows identifying three characteristic regions of the flow (see Fig.4): stagnation region, transition region and wall jet region where the local Nu number decreases monotonically.

By giving the best accuracy compared to Sagot *et al.* (2008) local Nusselt result, the SST k-ω is, then, used in the Average Nusselt number ($\overline{Nu}$) evaluation. So, a comparison between the current numerical results with the numerical, experimental and correlation ones found by Sagot *et al.* (2008) is performed and shown in Fig.5. This correlation is expressed as follows:

$$\overline{Nu} = 0.0603\,\mathrm{Re}^{0.8}\left[1-0.168\left(\frac{r}{D}\right)+0.008\left(\frac{r}{D}\right)^2\right]^{0.25}\left(\frac{H}{D}\right)^{-0.037}\left(\frac{\mu_j}{\mu_w}\right) \tag{13}$$

With limits interval:

10000≤Re≤30000 ; 3≤r/D≤10 ; 2≤H/D≤6

In the wall jet region, the numerical results of our model and the Sagot *et al.* (2008) model are very close to the experimental and correlation results proposed by Sagot *et al.* (2008). On the other hand, in the transition region, it can be noticed that our obtained numerical results are closer than the Sagot *et al.* (2008) numerical results to the experimental ones of Sagot *et al.* (2008). Thus, our numerical model allows to better predict the average Nusselt number. This improvement obtained using our numerical model can be explained by the fact that the SST k-ω model used in our simulations incorporates modifications and correction terms for the low Reynolds number effects, shear flow spreading, and compressibility, allowing a better reliability of the results.

- For a coaxial impinging jet, the numerical results of our model are compared to the numerical results of Celik *et al.* (2012) (coaxial jet) and to the correlation of Sagot *et al.* (2008) which is valid for coaxial and single jets in the wall jet region (Celik *et al.* 2012).

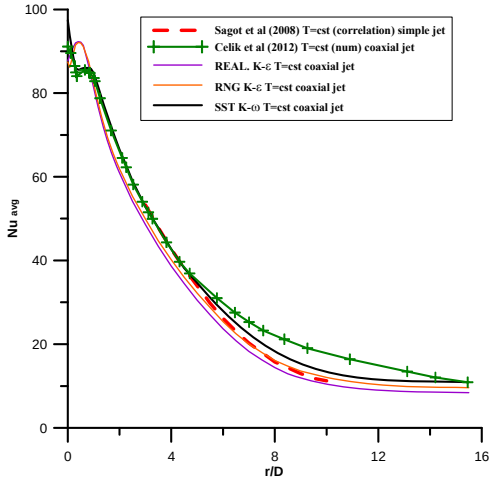

Fig. 6. Average Nusselt numbers ($\overline{Nu}$) of coaxial jet obtained with various turbulence models (case B) compared to literature results for d/D=0.35, H/D=4 and Re=10000.

Figure 6 shows the average Nusselt number distribution for a coaxial jet (H/D=4 and Re=10000), obtained using various turbulence models (case B in Table 3). By comparing our obtained SST k-ω model results to the numerical results found by Celik *et al.* (2012) in the stagnation and transition zones, it can be noticed that there is a good agreement. In the wall jet region, the coaxial impinging jet behaves like a single impinging jet (Celik *et al.* 2012). So, in order to validate our results in this region, a comparison with the Sagot *et al.* (2008) single impinging jet correlation results was established. It can be noticed

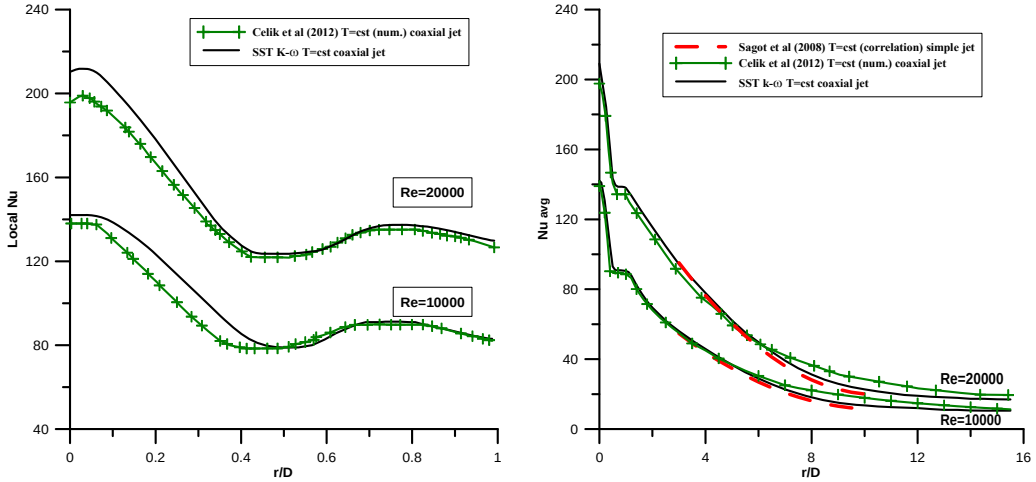

(a) **(b)**

Fig. 7. Nusselt number distributions (case C and D) compared to literature results for d/D=0.35, H/D=2 and (Re=10000 and Re=20000): (a) Local, (b) Average.

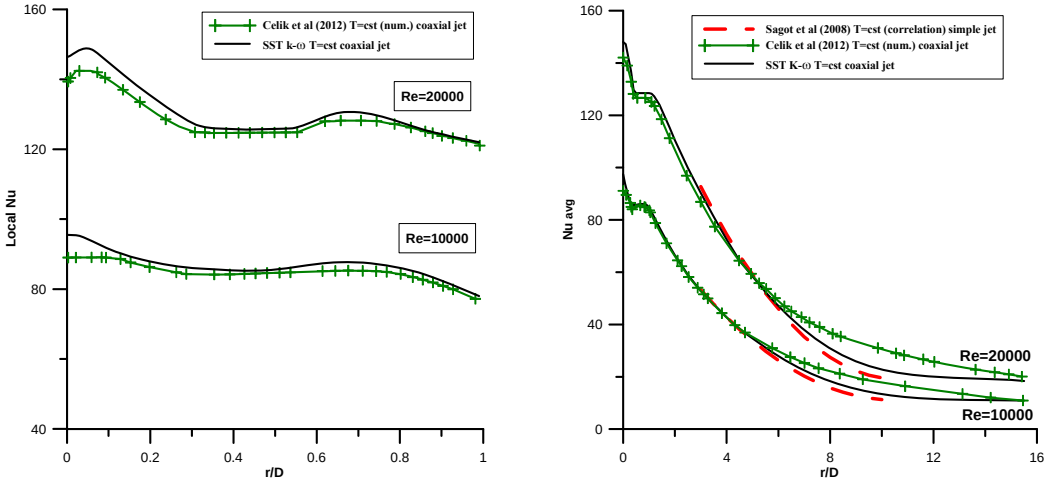

(a) **(b)**

Fig. 8. Nusselt number distributions (case B and E) compared to literature results for d/D=0.35 , H/D=4 and (Re=10000 and Re=20000): (a) Local, (b) Average.

that our obtained SST k-ω model results are closer than the numerical results of Celik *et al*. (2012) to the Sagot *et al*. (2008) correlation.

So, it can be deduced that our SST k-ω model results are generally in fair agreement with the average Nu of the single jet correlation found by Sagot *et al*. (2008) and an improvement has been achieved regarding the coaxial jet numerical results found by Celik *et al*. (2012).

It should also be noted that, even for the impinging coaxial jet, the RNG and Realizable k- ε models failed to predict correctly the flow. The SST k-ω model is adequate for flows having substantial regions of free shear/separation. Also, it joins merits of k-ε and k-ω formulations for the mixed, bounded and external flows. In the same context, several investigations have revealed that the SST turbulence model is the most appropriate to describe dynamically and thermally applications involving impinging jets (Sagot *et al*. 2008, Celik *et al*. 2012, Wang *et al*. 2014, Olsson *et al*. 2004, Casanova and Ortiz 2014).

Figures 7 and 8 illustrate the heat transfer of the impinging coaxial jet at the heated plate examined using the local Nu and the average Nu numbers. These Nusselt numbers are displayed for the jet exit-to-plate distances H/D of 2 and 4 and for Re=10000 and 20000 (case B, C, D and E).

Figures 7(a) and 8(a) present the distribution of the local Nu number. It can be seen that when the jet impinges the wall, a high heat transfer is obtained at the stagnation point. The same behaviour is also noticed for the circular single jets' cases. These figures also show that, in this configuration, a secondary maximum is located close to the stagnation point between r/D=0.6 and r/D=0.8. This latter becomes smaller with the increasing of H/D and the decreasing of Re.

A small deviation between our numerical results and those of Celik *et al*. (2012) is noted for all the H/D compared cases reaching 5%.

Figures 7(b) and 8(b) show the average Nusselt number results. It can be seen for all tested cases that, in the wall jet region, our numerical results are closer then the numerical results of Celik *et al*. (2012) to the Sagot *et al*. (2008) correlation. In the stagnation and transition zones, the agreement between the Celik *et al*. (2012) numerical results and our results is quite satisfactory for all tested Re numbers and H/D distances. Therefore, an improvement on the numerical result accuracy compared to Celik *et al*. (2012) results has been achieved.

- A comparison between a simple jet (d/D = 0) (case A) with a coaxial jet (d/D = 0.35) (case F) is shown in Fig.9. Celik *et al*. (2012) affirmed that, depending on the coaxial pipes diameter ratio, the impinging region of the jet differs. It can be observed, from Fig.9, that the coaxial jet with a diameter ratio d/D = 0.35 enables having a much higher heat transfer in the stagnation zone. This is an expected finding explained by the presence of the primary and secondary mixture streams of coaxial jets, which improves the potential core region and the turbulence intensity at the nozzle outlet. After a certain distance in the region of the parietal jet, r/D = 2.5, the results of the two cases merge while moving away from the stagnation zone, and the coaxial jet behaves like a single jet.

Finally, we can affirm that the different k- ε models cannot reproduce the real process on the stagnation zone. This zone is none other than the welding pool and the heat affected zone (HAZ) in the welding process. Therefore, the SST k-ω model is the most appropriate to deal with the considered problem and it will be used in the rest of this study.

3.2 Shielding gas Evaluation

Once the selected turbulence model for the flow field prediction has been validated, this model is applied in this section in order to reproduce accurately the laser welding and the shielding gas jet processes under the real operating conditions.

To remain within the validation interval of our model, Reynolds number is kept at a value of Re=10000. The same goes for the exit jet-to-wall distance kept at a value H/D=2. The gas jet role in this section is to protect the welding zone of the workpiece from oxidation. The selected laser beam power is equal to 1000W and is delivered perpendicularly to the workpiece (x-axis direction). The assist gas and the laser beam are immobilized and the workpiece moves on the y-axis with a velocity of 7m/min. This choice of the laser power and welding velocity were already validated by Bannour *et al*. (2012).

This section is devoted to investigate the efficiency of the shielding gas of the workpiece. Therefore, the study of the impact of different parameters on the shielding quality process and its zone extent has been carried out.

The studied parameters are as follows:

- Two different nozzles of the shielding gas: coaxial nozzles (d/D=0.35) and simple circular nozzle (d/D=0 and D=13.8mm).
- Two different inert shielding gases were taken into consideration in order to evaluate the density effect: Argon (ρ= 1.784 kg/m^{-3}), and Helium (ρ=0.178 kg/m^{-3}).
- Three different nozzle inclinations (θ) with respect to the laser beam axis: 0°, +45° (up), and -45° (down).
- Two welding directions (opposite workpiece movements): downward and upward.

The different studied cases in this section are summarized in Table 4.

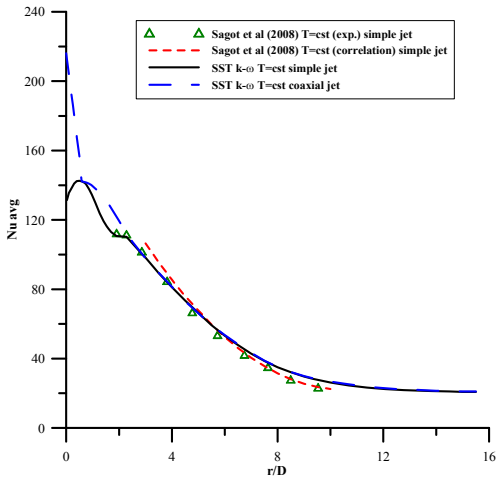

Fig. 9. Average Nusselt numbers ($\overline{Nu}$) of simple jet (case A) compared to coaxial jet (case F) and to simple jet experimental and correlation literature results for Re=23 000 and H/D=2.

Table 4 Different studied cases variable parameters

	Gas	Gas pipe geometry	Gas pipe inclination	Workpiece moving direction
Case 1	Argon	Simple	0°	From down to up
Case 2	Argon	Coaxial	0°	From down to up
Case 3	Argon	Coaxial	+45°	From down to up
Case 4	Argon	Coaxial	-45°	From down to up
Case 5	Argon	Coaxial	+45°	From up to down
Case 6	Argon	Coaxial	-45°	From up to down
Case 7	Helium	Coaxial	+45°	From up to down
Case 8	Helium	Coaxial	-45°	From down to up

It should be noted that the material ductility is greatly reduced by introducing the Oxygen into the shielding gas. Therefore, the higher the oxygen is, the more brittle the weld becomes. In order to investigate the shielded zone quality and its characteristic length, the distribution of the air volume fraction is discussed and calculated in the line (x=0, y, z=0), which represents the intersection of the workpiece's upper face and the symmetry plane (x,y). The characteristic lengths are compared between each

other at the same time t. It should be noted that, in all the studied cases, the coverage area is established.

Study of the coaxiality effect: The first part of the performed simulation task aims to evaluate the effect of the coaxiality.

Therefore, effects of coaxial nozzles and simple nozzle shielding gas jets on the air volume fraction distribution at the workpiece are compared (case1 and case 2). It is noted that: the used gas in those cases was Argon, the gas jets' inclination is θ=0° and the workpieces' movement is from down to up meaning that the weld pool is located at the positive part of the y-axis (the non-hatched area).
Figure 10 shows that in the two cases, the same air distribution profile is observed but there is a difference on the characteristic lengths. In fact, the coaxial nozzles' configuration promotes a better cover length compared to the simple nozzle. This improvement reached 25% with zero air volume fraction.

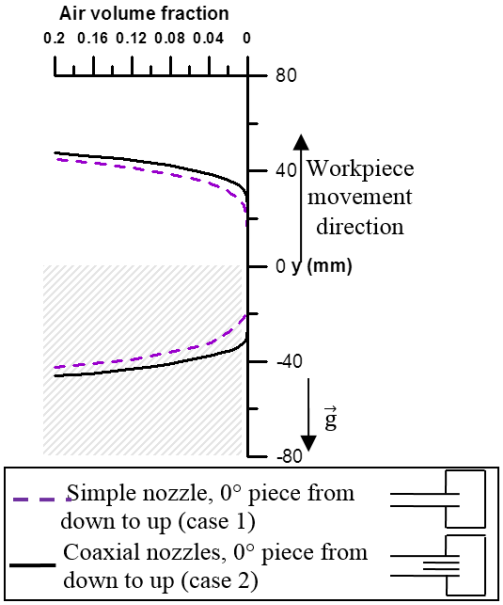

Fig. 10. Radial evolution of the air volume fraction for Argon single and coaxial jet.

Gas jet nozzles inclination effect: In order to understand the impact of the nozzle angle on the shielding zone characteristic length, the distribution of the air volume fraction for coaxial nozzles' configuration is presented in Figs 12, 13 and 14. In these figures, all of the angle positions are compared keeping in each figure the same movement direction of the workpiece. The test gas in those cases is Argon.

To better understand the difference between the cases 3, 4, 5 and 6, Fig.11 shows the location of the resultant welding pool which depends on the welding direction (workpiece motion direction), for each case. In the vertical welding process, the welding pool location (welding direction) affects the shielding gas distribution. In fact, the gas in contact with the heat affected zone (welding pool and solidification zone) sustains an upward motion due to the convective heat transfer.

Figure 12 shows the contours of the air volume fraction in the plane (x,y) for the coaxial nozzles' jet inclination angles θ= 0°, +45° and -45°. The presented cases are for the upward workpiece movement direction. Fig. 12 shows that the coverage of the laser beam impact zone is ensured for the three angles. Indeed, at the impact point O (x=0,y=0,z=0) (Fig. 12), the air volume fraction is equal to zero for the three inclination angles and this was confirmed by Fig. 13. On the other hand, it is noticed from Fig.12 that, far from the laser beam impact zone and in the Argon jet direction, the volume fraction contours are slightly different. This is due to the inclination of the injection nozzles and the effect of the inertia and buoyancy forces. This can be clearly observed in Figs.13 and 14.

Figure 13 shows the air volume fraction distribution on the line (x=0,y,z=0) of the same cases presented in Fig.12. In these cases (case 2, 3 and 4), the workpiece is in an upward movement direction, so the welding pool and heat affected zone are located at the positive part of the y-axis, as shown in Fig. 11. Focusing on this part of the y-axis (the non-hatched area in Fig.13), it can be noticed that for an air volume fraction under 0.05 the length of the gas covered area is: 104 mm in case 4 (θ=-45°), 40 mm in case 2 (θ=0°) and 19 mm in case 3 (θ=+45°). It is clear that the θ=-45° nozzle inclination (case 4) has the greatest covering length compared to other inclinations. It can be deduced that, the more the nozzle inclination decreases, the higher the covering characteristic length of the welding pool is. In fact, a large area of coverage is of great importance because it allows covering the welding pool and the solidification zone behind it. So, that protects the latter from oxidation and takes part in a fast solidification.

The area of the covered zone depends on three forces: the buoyancy forces due to the thermal and volume fraction gradient, the entrainment force due to the movement of the workpiece and the inertia force of the shielding gas jet. In case 4 (θ=-45°, workpiece from down to up), these three forces have the same direction which is upward (Fig. 11(b)). However, in case 3 (θ=+45°, workpiece from down to up), inertia force (downward) is impeded by buoyancy and entrainment forces (upward direction) (Fig. 11(a)). Therefore, the gas flow spread was hampered. Since these two cases (case 3 and 4) do not have the same phenomenon, they do not have the same evolution of air volume fraction.

In Fig.14, the workpiece moves from up to down which means that the welding pool is at the negative part of the y-axis (the non-hatched area). Focusing on this part of the y-axis, the covered zone of the θ=+45° nozzle inclination jet (case 5) matches with the welding pool placement contrary to the θ=-45° nozzle inclination jet (case 6) which covers the pre-weld zone. So, case 5 (θ=+45°) is preferable. On the other hand, the air volume fraction evolutions of cases 5 and 6 are almost axisymmetric with respect to the line y=0 (Fig. 14). This can be explained by the fact that: in case 5, the

entrainment and inertia forces acted in the opposite

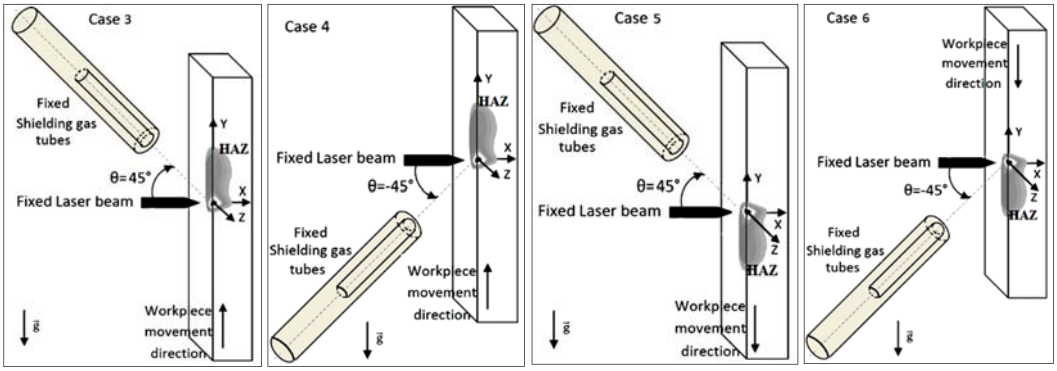

Fig. 11. Schematic and welding pool position of cases with inclined shielding gas nozzles: (a) case 3, (b) case 4, (c) case 5, (d) case 6.

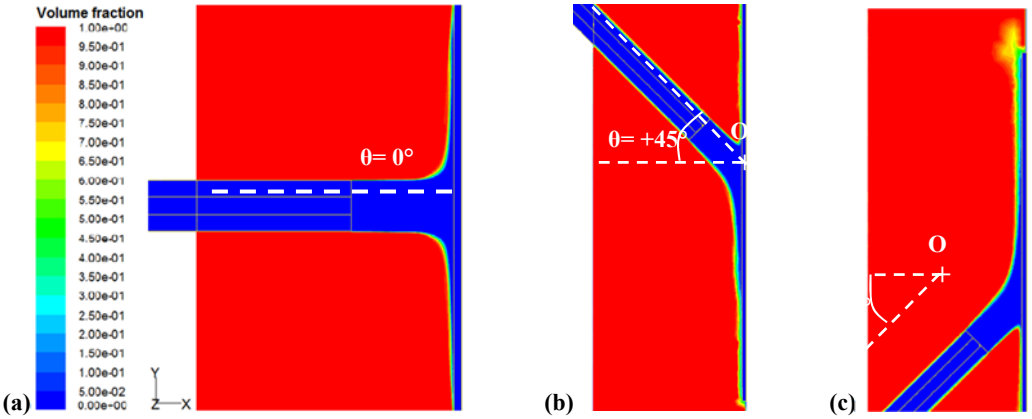

Fig. 12. Air volume fraction of coaxial nozzles Argon jet with workpiece movement from down to up at: (a) 0° of inclination (case 2), (b) +45° of inclination (case 3), (c) -45° of inclination (case 4).

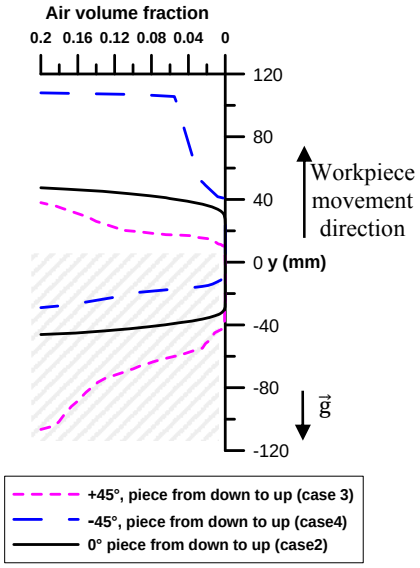

Fig. 13. Influence of Argon jet inclination for a workpiece moving from down to up

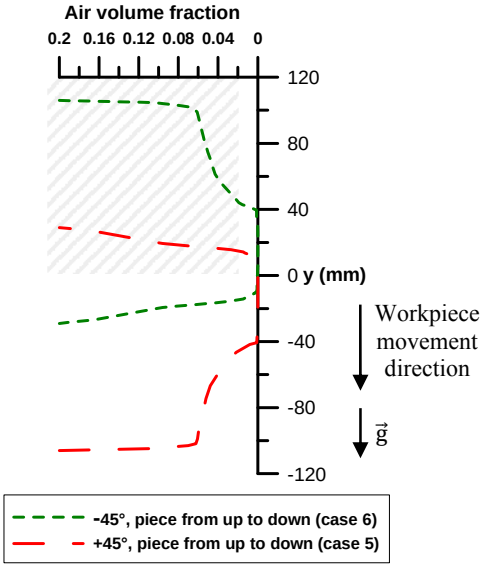

Fig. 14. Influence of Argon jet inclination for a workpiece moving from up to down

direction of the buoyancy forces, and, in case 6, buoyancy and inertia forces proceed in the opposite direction of the entrainment force of the workpiece. This means that in both cases, among the three forces, there is constantly one that goes with the jet inertia force in its direction.

So, it can be concluded from Figs. 13 and 14 that the

two cases which succeeded in ensuring a good gaseous coverage of the welding pool and the solidification zone are case 4 (-45°, piece from down to up) and case 5 (+45°, piece from up to down). This means that for a good coverage area the entrainment force due to the movement of the workpiece and the inertia force of the shielding gas jet should proceed in the same direction.

Welding direction effect: As shown in Fig. 11, the welding direction sets the position of the heat affected zone on the workpiece. Since the HAZ and the vertical position of the workpiece effect the shielding gas jet distribution, the welding direction is of a significant importance. In order to study its impact on the length shielded zone, a comparison between the results of the two best cases previously found (cases 4 and 5) is performed. To properly compare the two evolutions of the air volume fraction, we reversed in Fig. 15 the profile corresponding to case 5. So, Fig. 15 shows the air volume fraction distribution of the cases 4 (-45°, piece from down to up) and 5 (+45°, piece from up to down). An improvement on the coverage zone is noticed by moving the workpiece in upward direction in case 4, compared to case 5 where the workpiece moves in downward direction. In fact, case 5 (θ=+45°) ensures a coverage length of □y□=72 mm with an air volume fraction less than 0.05 against □y□=104 mm in case 4 (θ=-45°). This improvement can be explained by the fact that, in case 5 (θ=+45°, workpiece from up to down), inertia and the entrainment forces move in a downward direction, and they are impeded by buoyancy forces which have an upward direction. This represents a disadvantage for case 5 compared to case 4 where inertia, entrainment and buoyancy forces are in the same direction. The movement of all forces in the same direction improved the Argon gas jet evolution and therefore the coverage length shown in Fig. 15.

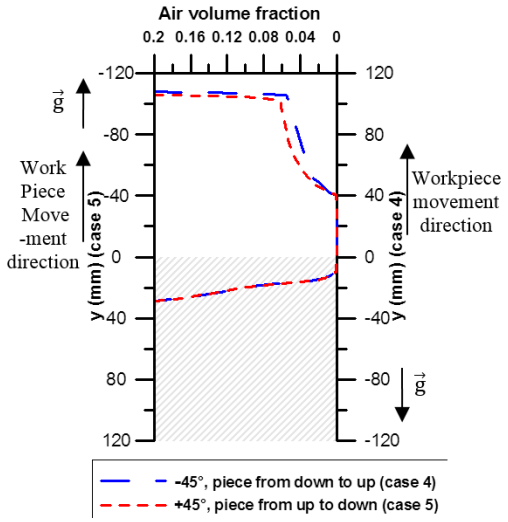

Fig. 15. Influence of the workpiece moving direction.

So, the combination in case 4 of the coaxial nozzles' jet inclination of θ=-45° with the upward workpiece movement direction and Argon gas gives the best length of the shielded area of the welding pool and the solidification zone.

Shielding gas type effect: In this last part, attention is paid to the shielding inert gas type effect. The choice of the latter affects significantly the coverage of the welding pool.

In order to evaluate the impact of different gas densities, the Argon gas is compared to a lower density gas: Helium. Air volume fractions at the workpiece are compared for both gas types, with the same coaxial nozzles' inclinations and the same moving workpiece direction. This comparison is treated for both combinations which gave a good shielding process with the Argon gas (cases 4 and 5).

It is noticed that Helium has a different behaviour as it disperses quickly in the environment. The Helium gas has a tendency to disperse in the air more than Argon. This finding can be noticed by comparing the profiles in the two figures: Figs.16 (a) and (b) which show the air volume fraction fields on the (x,y) plane.

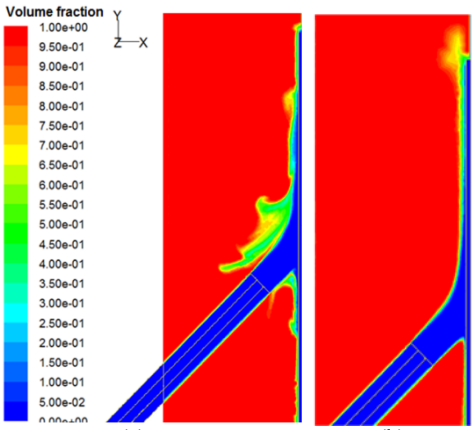

Fig. 16. Air volume fraction of coaxial nozzles jet with inclination θ =-45° and upward workpiece movement direction: (a) Helium (case2), (b) Argon (case 4).

Figure 17 shows the air volume fraction distribution for a θ=+45° nozzles' inclination of both gas types with a downward workpiece movement direction (cases 5 and 7).

The dispersion of the Helium enables to obtain a larger extent of the shielding zone on the positive part of the y-axis (hatched area). But this is the pre-weld zone. So, it is useless. On the other part of the y-axis corresponding to the region of the welding pool and the solidification zone, Helium gas ensures a better protection quality until the position of y=-72 mm with an air volume fraction of 0.05. Beyond this distance, the air volume fraction increased more roughly than that with the Argon gas. Meaning beyond y =-72mm, Helium gas's protection quality decreased more significantly than the Argon's. The latter enables having an air volume fraction of 0.07 at y= -103mm against 0.17 at the same distance with the Helium gas.

Figure 18 presents a comparison between case 4 using Argon gas and case 8 using Helium gas for an inclination of θ=-45° and a workpiece movement direction from down to up.

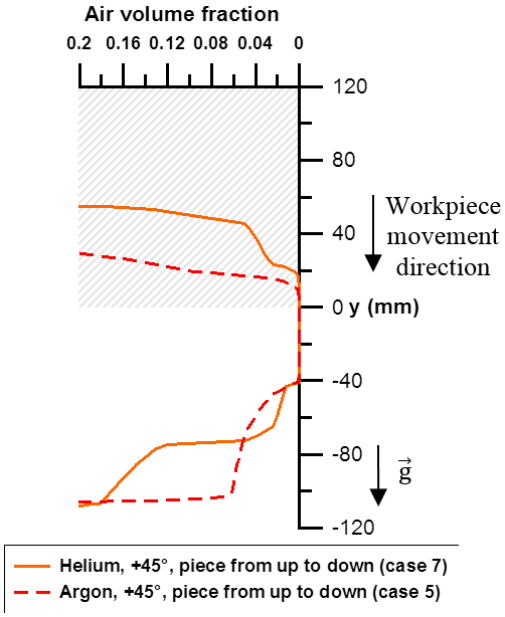

Fig. 17. Influence of gas type for nozzles inclination θ=+45° and downward workpiece movement direction.

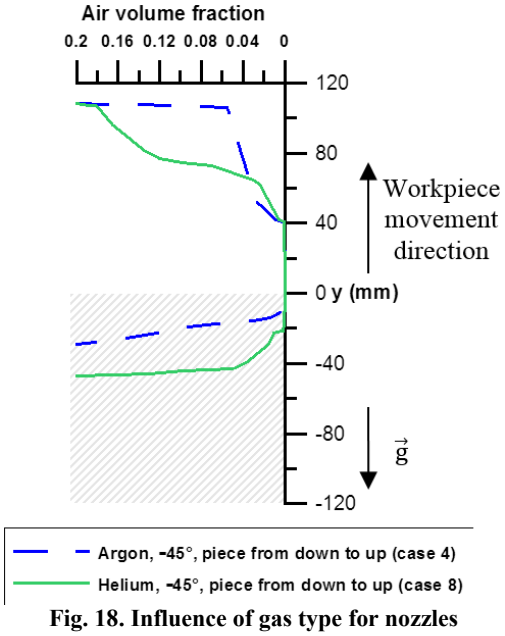

Fig. 18. Influence of gas type for nozzles inclination θ= -45° and upward workpiece movement direction.

Similarly to Fig.17 results, in the pre-weld zone (negative part of y-axis (hatched area)) Helium has a larger coverage zone than Argon. But in the welding and solidification zone, the Helium succeeded in ensuring a better protection quality until y = 65mm with an air volume fraction of 0.035. From this y value, the protection decreased more rapidly than that with the Argon gas. The latter allows having an air volume fraction of 0.055 at y = 106 mm against 0.18 at the same distance with the Helium gas.

Therefore, it can be concluded that, the adequate solution for the largest gas covered zone is that of the case 4. That means using the Argon as a shielding gas, a coaxial jet nozzles with an inclination angle of θ=-45° and an upward workpiece movement direction, which corresponds to a downward welding direction.

4. CONCLUSION

A three dimensional computational study was conducted in order to investigate the impact of different geometrical parameters of a vertical welding process relevant to the shielding supplying jet nozzles, the shielding gas type and the welding direction, on the shielding quality process and its zone extent. The laser beam power during the welding is simulated using a Gaussian volumetric heat source. The CFD model, developed using the SST k-ω as a turbulence model, allowed to reproduce accurately the welding process and assess properly the evolution of the coverage zone.

According to the results, significant conclusions could be drawn:

- The configuration of the coaxial gas nozzles promotes a greater length of coverage than the single nozzle reaching 25%.
- For a downward welding direction, as the inclination of the assist gas nozzle decreases, the covering characteristic length increases, and for an upward welding direction, the opposite is noticed.
- Because of the upward effect of the heat caused by the welding zone, the parametric combination of the welding direction (downward) and the smallest inclination (θ=-45°) of the assist Argon gas nozzle turns out to be better than the other cases ensuring a larger shielding zone extent.
- The argon gas remains better than the Helium gas to provide a larger covering characteristic length, despite the fact that the latter has succeeded in giving a better protection quality until a certain length.

As known, the welding pool shape and the solidification zone are mainly affected by the shielding gas parameters, the next study will be focused on these process parameters. The effect of the variable thermal properties of the workpiece material will also be investigated.

REFERENCES

Abderrazak, K., S. Bannour, H. Mhiri and G. Lepalec, M. Autric (2009). Numerical and experimental study of molten pool formation during continuous laser welding of AZ91magnesium alloy. *Comput. Mater. Sci.* 44(3), 858–66.

Akbari, M., S. Saedodin, D. Toghraie, R. Shoja

Razavi and F. Kowsari (2014). Experimental and numerical investigation of temperature distribution and melt pool geometry during pulsed laser welding of Ti6Al4V alloy. *Opt. Laser Technol.* 59, 52–59.

Ancona, A., T. Sibillano, L. Tricarico, R. Spina, P. M. Lugara, G. Basile and S. Schiavone (2005). *J. Mat. Process. Technol.* 164–165, 971–77.

Bahiraei, M. (2016). Particle migration in nanofluids: A critical review. *Int J Therm Sci* 109, 90-113.

Bahiraei, M., R. Khosravi and S. Heshmatian (2017). Assessment and optimization of hydrothermal characteristics for a non- Newtonian nanofluid flow within miniaturized concentric-tube heat exchanger considering designer's viewpoint. *Appl. Therm. Eng.* 123, 266-276.

Bahiraei, M., S. M. Hosseinalipour and M. Hangi (2014). Heat transfer and flow characteristics of nanofluid in a narrow annulus: numerical study, modelling and optimisation*, Can. J. Chem. Eng.* 92, 747- 757.

Bahiraei, M., S. M. Naghibzadeh and M. Jamshidmofid (2017). Efficacy of an eco-friendly nanofluid in a miniature heat exchanger regarding to arrangement of silver nanoparticles. *Energ. Convers. Manage.* 144, 224–234.

Bannour, S., K. Abderrazak, H. Mhiri and G. LePalec (2012). Effects of temperature-dependent material properties and shielding gas on molten pool formation during continuous laser welding of AZ91 magnesium alloy. *Opt. Laser Technol.* 44, 2459–68.

Bennon, W. D. and F. P. Incropera (1987). A continuum model for momentum, heat and species transport in binary solid–liquid phase change systems model formulation. *Int. J. of Heat Mass Tran.* 30, 2161–70.

Buchlin, J. M. (2011). Convective Heat Transfer in Impinging Gas Jet Arrangements. *J. Appl. Fluid. Mech.* 4(2),1, 137-149.

Cao, X., M. Jahazi, J. P. Immarigeon and W. Wallace (2006). A review of laser welding techniques for magnesium alloys. *J. Mat. Process. Technol.* 171, 188–204.

Casanova Ortega, J. and F. J. Granados Ortiz (2014). Numerical simulation of the heat transfer from a heated plate with surface variations to an impinging jet, *Int. J. Heat Mass Tran.* 76, 128–43.

Celik, N. and D. W. Bettenhausen (2012). Numerical investigation of the co-axial impinging jets with various diameter ratios. *J. Enhanc. Heat Transf.* 19(2), 135–47.

Celik, N. and H. Eren (2009). Heat transfer due to impinging co-axial jets and the jets' fluid flow characteristics. *Exp. Therm. Fluid Sci*. 33, 715-27.

Chang, B., C. Allen, J. Blackburn and P. Hilton (2013). Thermal and fluid flow characteristics and their relationships with porosity in laser welding of AA5083, *Physcs. Proc.* 41, 478 – 87

Cho, D., W. Cho and S. Na (2014). Modeling and simulation of arc: Laser and hybrid welding process, *J. Manuf. Process.* 16, 26–55.

Choudhury, D. (1993). Introduction to the renormalization group method and turbulence modeling. *Fluent Inc. Technical Memorandum* TM-107.

Fan, H. G., H. L. Tsai and S. J. Na (2001). Heat transfer and fluid flow in a partially or fully penetrated weld pool in gas tungsten arc welding. *Int. J. Heat Mass Tran.* 44, 417–28.

Goldak, J., A. Chakravarti and M. Bibby (1984). New finite element model for welding heat sources. *Metall. Trans. B* 15(B), 299–305.

Grevey, D., P. Sallamand, E. Cicala and S. Ignat (2005). Gas protection optimization during Nd:YAG laser welding. *Opt. Laser Technol.* 37(8), 647–651.

Ha, E. J. and W. S. Kim (2005). A study of low-power density laser welding process with evolution of free surface. *Int. J. Heat Fluid Fl.* 26, 613–21.

Haferkamp, H., M. Niemeyer, U. Dilthey **and** G. Trager (2000). Laser and electron beam welding of magnesium materials. *Weld. Cutt.* 52(8),178–80.

Hozoorbakhsh, A., M. I. S. Ismail, A. A. D. M. Sarhan, A. Bahadoran and N. B. AbdulAziz (2016). An investigation of heat transfer and fluid flow on laser micro-welding upon the thin stainless steel sheet (SUS304) using CFD, *Int. Commun. Heat Mass* 75, 328–340.

International Magnesium Association, (*www.intlmag.org)*.

Jambunathan, K., E. Lai, M. A. Moss and B. L. Button (1992). A review of heat transfer data for single circular jet impingement. *Int. J. Heat Fluid Fl.* 13(2).

Lee, J. and S. Lee (2000). The effect of nozzle configuration on stagnation region heat transfer enhancement of axisymmetric jet impingement. *Int. J. Heat Mass Tran.* 43, 3497-3509.

Li, X., F. Lu, H. Cui, X. Tang and Y. Wu (2014). Numerical modeling on the formation process of keyhole-induced porosity for laser welding steel with T-joint. *Int. J. Adv. Manuf. Technol.*

Limmaneevichitr, C. and S. Kou (2000). Experiments to simulate effect of Marangoni convection on weld pool shape. *Weld J.* 79, 231s–37s.

Lin, Y. C. and P. Y. Chen (2001). Effect of nitrogen content and retained ferrite on the residual stress in austenitic stainless steel weldments. *Mater. Sci. Eng. A* 307, 165–71.

Meena, H. C., S. A. Reodikar, R. Vinze and S. V. Prabhu (2016). Influence of the shape of the orifice on the local heat transfer distribution between smooth flat surface and impinging incompressible air jet. *Exp. Therm. Fluid Sci.* 70, 292–306.

Menter, F. (1994). Two-equation eddy-viscosity turbulence models for engineering applications. *AIAA J.* 32, 1598–1605.

Muthukannan, M., P. Rajesh Kanna, S. Jeyakumar and A. Bajpai (2016). Flow field and heat Transfer investigation of a confined laminar slot air jet on a solid block. *J. Appl. Fluid. Mech.* 9(4), 1679-94.

Olsson, E. E. M., L. M. Ahrné and A. C. Tragardh (2005). Flow and heat transfer from multiple slot air jets impinging on circular cylinders. *J. Food Eng.* 67, 273–280.

Qiang, W., X. Lanying and M. Yong (2014). Melted characteristics effects of shielding gas on laser deep penetration welding. *Key Eng. Mat.*620, 116-121.

Sagot, B., G. Antonini, A. Christgena and F. Burona (2008). Jet impingement heat transfer on a flat plate at a constant wall temperature. *Int. J. Therm. Sci.* 47, 1610–19.

Sathiya, P., K. Panneerselvam and R. Soundararajan (2012). Optimal design for laser beam butt welding process parameter using artificial neural networks and genetic algorithm for super austenitic stainless steel. *Opt. Laser Technol.* 44, 1905–1914.

Shih, T. H., W. Liou, A. Shabbir, Z. Yang and J. Zhu (1995). A new k- ε eddy-viscosity model for high reynolds number turbulent flows model development and validation. *Comput. Fluids,* 24(3), 227-38.

Sun, J., P. Nie, K. Feng, Z. Lia, B. Guo and E. Jiangc (2017). The elimination of pores in laser welds of AISI 304 plate using different shielding gases. *J. Mater. Process. Tech.* 248, 56–63.

Tani, G., A. Ascari, G. Campana and A. Fortunato (2007). A study on shielding gas contamination in laser welding of non-ferrous alloys. *Appl. Surf. Sci.*254, 904–07.

Trinh, X. T., M. Fénot and E. Dorignac (2016). The effect of nozzle geometry on local convective heat transfer to unconfined impinging air jets. *Exp. Therm. Fluid Sci.*70, 1-16.

Voller, V. R. and C. Prakash (1987). A fixed grid numerical modelling methodology for convection-diffusion mushy region phase-change problems. *Int. J. Heat Mass Tran.* 30(8), 1709-19.

Wang, H., Y. Shi, S. Gong and A. Duan (2007). Effect of assist gas flow on the gas shielding during laser deep penetration welding. *J. Mater. Process. Technol.* 184,379–385.

Wang, P., J. Lv, M. Bai, Y. Wang and H. Chengzhi (2014). Numerical investigation of the flow and heat behaviours of an impinging jet. *Int. J. Comput. Fluid.*

Wang, R., Y. Lei and Y. Shi (2011). Numerical simulation of transient temperature field during laser keyhole welding of 304 stainless steel sheet. *Opt. Laser Technol*. 43(4), 870–73.

Yokoharaa, K., Y. Okamotoa, A. Okadaa, H. Ochiaib, R. Kimurab and M. Akase (2016). Investigation of shielding gas supplying method in vertical-position laser welding of pure titanium. *Procedia CIRP* 42, 448–53.